Supporting Information:

Embedding PbS QDs in Pb-halide perovskite matrices: QD Surface chemistry and antisolvent effects on QD dispersion and confinement properties

E. Ashley Gaulding,[1,2*] Xihan Chen,[1,2] Ye Yang,[1,2] Steven P. Harvey,[2] Bobby To,[2] Young-Hoon Kim,[1,2] Matthew C. Beard,[1,2] Peter C. Sercel,[1,3*] Joseph M. Luther[1,2*]

[1] Center for Hybrid Organic Inorganic Semiconductors for Energy (CHOISE)

[2] National Renewable Energy Laboratory, Golden, CO USA

[3] Department of Applied Physics and Materials Science, California Institute of Technology, Pasadena, CA USA

[*] Corresponding authors

Materials: All chemicals were used as purchased without further purification. Purchased from Sigma-Aldrich: Lead(II) oxide (PbO, 99.999%), lead(II) chloride ($PbCl_2$, 99.999%), lead(II) bromide ($PbBr_2$, 99.999%), lead(II) thiocyanate ($Pb(SCN)_2$, 99.5%), oleic acid (OA, technical grade 90%), oleylamine (OLA, technical grade 70%), 1-octadecene (ODE, technical grade 90%), N,N-Dimethylformamide (DMF, 99.8%, anhydrous), dimethyl sulfoxide (DMSO, >99.9%, anhydrous), toluene (99.8%, anhydrous), hexane (reagent grade ≥95%), ethanol (EtOH, 200 proof, ≥99.5%), methyl acetate (MeOAc, anhydrous 99.5%), chlorobenzene (CB, 99.8%, anhydrous), anisole (AN, 99.7%, anhydrous), tetrachloroethylene (TCE, >99.9%), bis(trimethylsilyl) sulfide (TMS-S, 98%). Purchased from Alfa Aesar: lead (II) iodide (PbI_2, 99.9985%). Purchased from Greatcell Solar Materials: methylammonium iodide (MAI, >99%), methylammonium bromide (MABr, >99%).

Experimental Details:

PbO Synthesized PbS: PbS QDs were synthesized using previously reported methods[1] with some variations. In short, a solution of oleic acid (OA), lead (II) oxide (PbO), and 1-octadecene (ODE) were heated to 120C and degassed under vacuum on a Schlenk line for 1 hour. This solution was then raised (or lowered) to a given temperature for injection of an anhydrous TMS_2-S/ODE solution and allowed to react for 30 secs before removing the heating mantel and allowing the solution to cool. The QDs were then precipitated with ethanol and centrifuged at 8000 rpm for 5 min. The QD pellet was then redispersed in hexane and precipitated again. The QDs were finally redispersed in hexane and stored in a dry box. A combination of different Pb-oleate/ TMS_2-S ratios and injection temperatures resulted in different sized QDs as summarized in the table below. The size of the PbS was determined using the first exciton peak of the absorption spectra of the as-synthesized, OA capped NCs in tetrachloroethylene (TCE) based on previous literature.[2]

Table S1: PbO Synthesized PbS Conditions

QD Dia. (nm)	1st Exciton (nm)	PbO (mg)	TMS-S (µL)/ ODE (mL)	OA (g)	ODE (g)	Injection T (°C)

1.9	632	460	150/5	2.1	2.5	50 (rxn 1 min, then quench w/ 10mL *cold* anhydrous ethanol)
2.1	680	460	150/5	2.1	2.5	50 (rxn 1 min, then quench w/ 10mL anhydrous ethanol)
2.5	784	950	420/10	3	20	75 (then ice bath quench)
2.8	864	950	420/10	3	20	85
3.3	989	900	420/10	4	20	120
4.8	1345	900	420/10	28	20	95

PbCl$_2$ Synthesized PbS: PbCl$_2$ based QDs were synthesized following a previously published procedure.[3] 10 mL of OLA and 3 mmol (0.8343 g) of PbCl$_2$ were added to a three-neck flask and degassed on a Schlenk line under vacuum at 80°C for ~ 1hr. The flask was then placed under nitrogen and heated at 140°C for 30 min. The solution was then allowed to cool to 30°C, and a solution of 210 µL TMS-S, 2 mL OLA was injected once the solution was reheated to the desired growth temperature (see Table S3), and immediately quenched in a water bath. The reaction solution was then split equally into two 50 mL centrifuge tubes. Ethanol was added as an antisolvent to each tube up to the 45 mL mark, then the tubes were centrifuged at 8000 rpm for 5 min. The supernatant was decanted, and the remaining pellet was redispersed in ~5 mL of hexane, plus 6 mL of OA to help with colloidal stabilization. This solution was stored in a nitrogen flow box for 24 hrs to allow any unreacted PbCl$_2$ to precipitate. The solution was then run through a 0.2 µm PTFE filter, and finally purified three times using ethanol/hexane as the antisolvent/solvent pair as before (but not adding OA). The final QD solution in hexane was stored in a nitrogen flow box.

Table S2: PbCl$_2$ Synthesized PbS Conditions

QD Dia. (nm)	1st Exciton (nm)	PbCl$_2$ (mg)	TMS-S (µL)/ OLA (mL)	OLA (g)	ODE (g)	Injection T (°C)
2.4	764	834	210/2	10 mL	N/A	70
2.7	856	834	210/2	10 mL	N/A	90
3.3	984	834	210/2	10 mL	N/A	110
3.5	1038	834	210/2	10 mL	N/A	130
4.0	1175	834	210/2	10 mL	N/A	150

MAI/PbI$_2$ solution exchange: The solution exchange follows a previously published procedure.[4,5] The stock PbS solution is diluted to 5 mg/mL (PbS in hexane). 1.125 – 0.8 mL of MAI/PbI$_2$ exchange solution is added per ml of PbS/hexane (5 mg/mL) solution. Smaller diameter QDs need more exchange solution relative to larger QDs. The solution is vortexed for ~15 secs and then allowed to phase separate. The now clear/colorless hexane phase (top) is removed via pipette. The same amount of pristine hexane (no ligand) is added back to the solution and this process is repeated twice. The PbS QDs, now in the MAI/PbI$_2$ exchange solution, are then precipitated with toluene and centrifuged (8000 rpm, 5 min). The clear yellow supernatant is thoroughly discarded. This precipitation process can be repeated a second time by redispersing the PbS in pure DMF and again precipitating with toluene, but we found if the QDs are over washed or the pellet is allowed to completely dry, that the QDs were not as easily dispersed in the precursor solution. Therefore, the PbS pellet is immediately brought into a nitrogen glovebox and quickly redispersed into the perovskite precursor solution (prepped in the glovebox) at the desired concentration. The perovskite precursor solution recipe is 0.922g (2 mmol) PbI$_2$, 0.318g (2 mmol) MAI, 0.022g Pb(SCN)$_2$, 1.26mL DMF, 0.140mL DMSO. The solution was vortexed inside the glovebox until fully dissolved. The QD/perovskite

precursor solution used for spin-coating the dot-in-matrix films was kept at a constant concentration on a molar basis in order to keep the total number of QDs per volume of solution the same across solutions with different sized QDs. The mass-based concentration of QDs per volume was calculated for the stock solution based on solution absorption measurements using previous published methods.[2] This number was then converted to a QD/volume bases by approximating the QDs as a sphere and using the density of PbS. The concentration used was $1.3*10^{18}$ QD/mL, which converts to $36 - 576$ mg/mL depending on the QD size. As is implied, the exchanged QDs are highly soluble in the perovskite precursor solution.

Table S3: Conditions for different MAPI crystallization antisolvent treatments.

	Methyl Acetate	Chlorobenzene	Anisole
Spin speed (rpm)	3000	3000	3000
Total spin time (s)	30	30	30
Time of antisolvent drip	After 9 sec	After 9 sec	dipped 5 sec
Volume of antisolvent (uL)	200	200	immersed
Anneal	100°C, 5 min	100°C, 5 min	60°C 3 min; then 100°C 5 min

Absorption: For solutions, absorption measurements were taken with a Shimadzu UV-3600 UV-vis-NIR spectrophotometer with the given solvent as the baseline. For films, both transmission and reflection measurements were taken using a Cary 6000i UV-vis-NIR spectrometer with a DRA 150mm integrating sphere accessory. Data was baselined to the substrate (glass) and the absorption determined by subtracting %T and %R from 100%.

Photoluminescence: PL data was taken using an Ocean Optics setup using a cuvette holder for solution and reflectance probe for films. OceanFX and NIRQuest detectors collected the UV-Vis and NIR data, respectively. Samples were excited using a pulsed $\lambda_{exc} = 405$ nm LED and controller (Thor Labs).

TOF-SIMS: An ION-TOF TOF-SIMS V Time of Flight SIMS (TOF-SIMS) spectrometer was utilized for depth profiling and chemical imaging of the perovskite utilizing methods covered in detail in previous reports.[6–8] Analysis was completed utilizing a 3-lens 30kV BiMn primary ion gun. High mass resolution depth profiles were completed with a 30KeV Bi^{3+} primary ion beam, (0.8pA pulsed beam current), a 50x50µm area was analyzed with a 128:128 primary beam raster. 3-D tomography and high-resolution imaging was completed with a 30KeV Bi^{3+} primary ion beam, (0.1pA pulsed beam current), a 25x25µm area was analyzed with a 512:512 primary beam raster. In both cases the primary ion beam dose density was kept below 1×1012 ions cm−2 to remain under the static-sims limit). Sputter depth profiling was accomplished with 1kV Cesium ion beam (7 nA sputter current) with a raster of 150×150 microns. After completion of the SIMS measurements the depth of the sputtered craters was determined by optical interference light microscopy, to convert the SIMS sputter time scale to a sputter depth scale.

SEM: A FEI Nova 630 Electron Microscope was used to profile and characterize your films. Sample mounting utilized carbon adhesive paint, Electrodag 502, with a small amount touching the surface of the films to create a conduction path to dissipate charge build up. Samples may have been coated with 15 seconds of Au/Pd film to further mitigate charging effects. Samples were then imaged under lower energy, small working distance range (between 3-7mm) and low current settings to minimize beam damage, and to emphasize surface texturing my mitigating edge effects that occur at high energy/high current conditions.

Characterization at low and high magnification allowed for a more comprehensive breakdown of material grain size, roughness, and overall surface contouring.

Transient Absorption: Transient absorption spectra were collected using a Coherent Libra Ti:sapphire laser, with an output of 800 nm at 1kHz. The 800 nm beam was directed into a TOPAS optical parametric amplifier to generate pump pulse (~150 fs) at 500 nm and was modulated at 500 Hz through an optical chopper to block every other laser pulse. Femtosecond TA spectra were collected using Helios spectrometer (Ultrafast Systems). A small amount of 800 nm light was used to pump a sapphire crystal to create 450 – 800 nm probe light for TA.
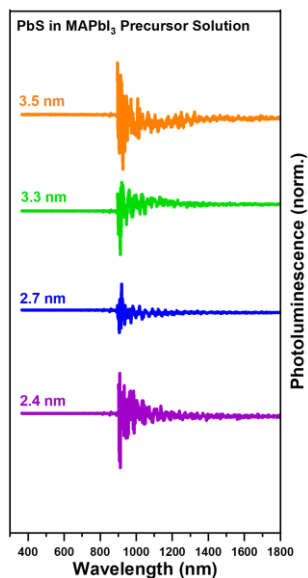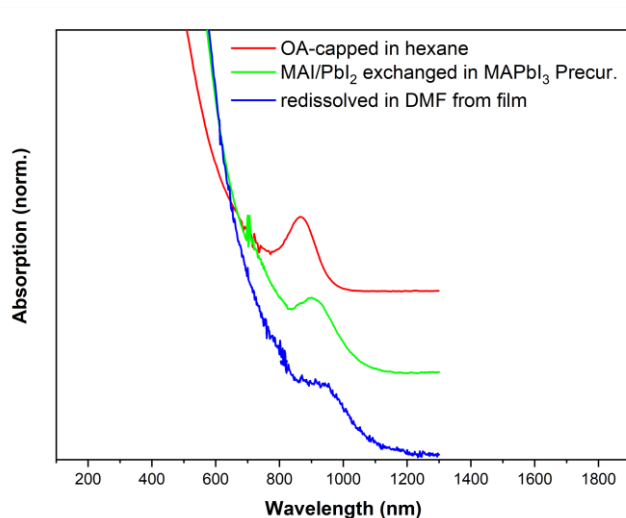
Additional Figures
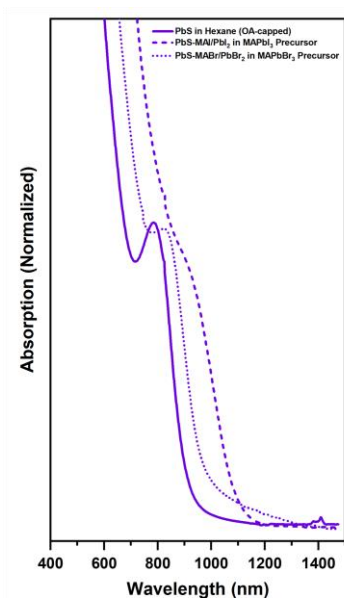
Figure S1: Comparison of small PbS exchanged into $MAPbI_3$ (dashed line), versus $MAPbBr_3$ (dotted line) precursor solutions, demonstrating smaller red shift and a more defined exciton with the $MAPbBr_3$ precursor.
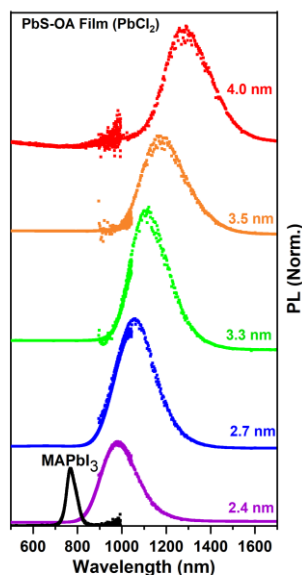
**Figure S2**: PL from PbS-OA films, with $MAPbI_3$ for reference.

Figure S3: PL measurement of PbS_{PbCl2} NCs in $MAPbI_3$ precursor solution.

Figure S4: Absorption measurements showing the starting PbS exciton peak (red), the peak after the QDs are first dispersed into the MAPbI$_3$ precursor solution (green), then the same QDs after they've been crystallized in a MAPbI$_3$ film and then redissolved into DMF (blue), indicating the size of the PbS is maintained.
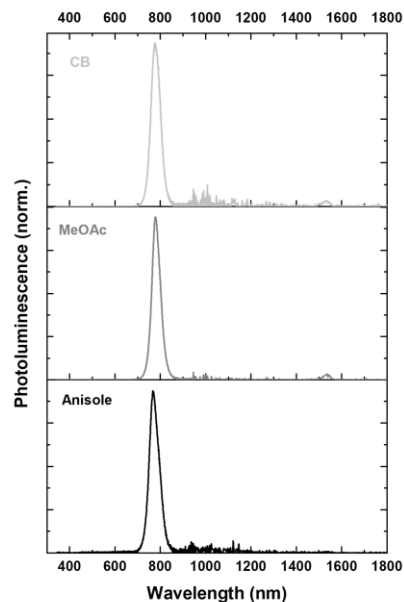
Figure S5: PL of MAPbI$_3$ only films using the different antisolvent treatments. The small peak at ~1530 nm is from erbium dopant in the fiber optic cable.
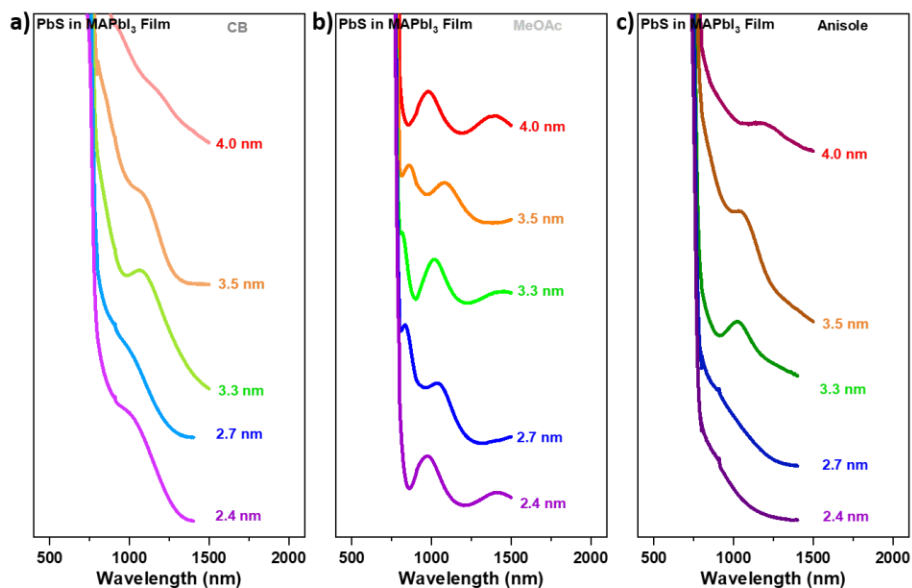
Figure S6: Absorption data of PbS$_{PbCl2}$/MAPbI$_3$ films crystallized using the methods, a) CB drip, b) MeOAc drip, c) AN dip. The MeOAc drip films show a large reflectance interference pattern, making it

difficult to distinguish the PbS exciton peak, despite taking both transmission and reflectance measurements of the film to calculate absorption. Curves are offset for clarity.
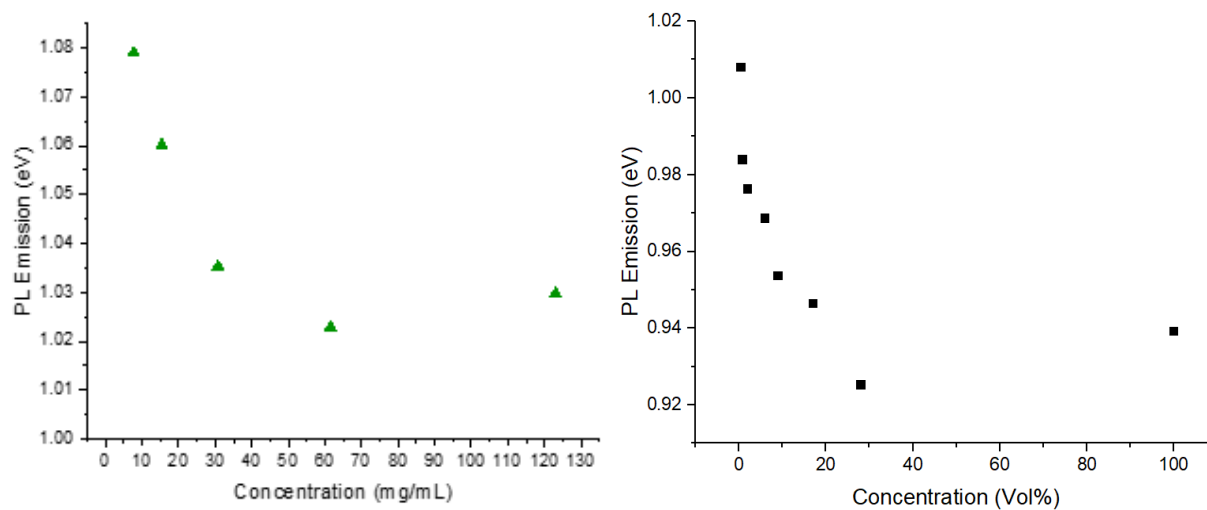
Figure S7: PL Emission dependent on PbS concentration for a) 3.3nm PbS synthesized in for this study and b) 4.5nm PbS plotted from emission data published by Sargent et al.[9]
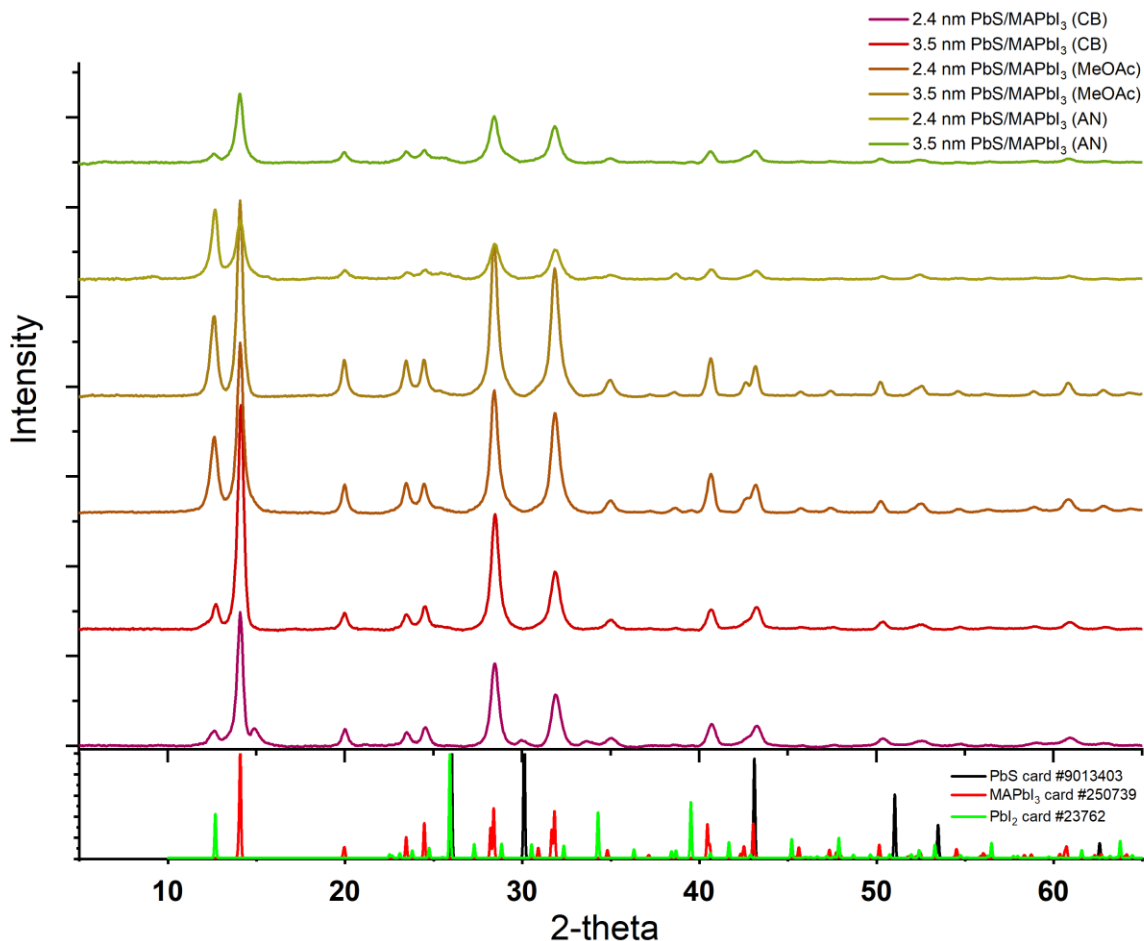
Figure S8: XRD data of PbS/MAPbI3 films with different sizes and antisolvent treatments. PbS is a small fraction of the overall film, thus the PbS peaks are difficult to resolve.

Calculation of strain for a spherical PbS QD in MAPI matrix and effect on electronic properties.

A PbS QD embedded in a matrix of MAPI (MAPbI$_3$) will be strained if the interface between the QD and the surrounding matrix is atomically coherent. This is because the bulk lattice constants of PbS and MAPI are different: If the interface is assumed to be atomically coherent, the lattice on each side of the interface must be strained in order to achieve lattice matching at the interface. The precise degree of strain in each material will be dependent on the bulk lattice parameters and the elastic response of the two materials. The solution to the problem of strain associated with a spherical inclusion in an infinite matrix was first described by Eshelby using continuum elasticity theory.[10] Eshelby's inclusion theory was applied to the specific problem of coherent epitaxial strain of a spherical crystalline inclusion in a crystalline matrix by Yang et al.[11] To determine the strain in the PbS/MAPI dot-in-matrix samples grown in this study, we applied the theory of Yang et al.,[11] assuming a spherical shape for the PbS QDs and assuming that the lattice interface between the PbS QD and the MAPI matrix is coherent.[9]

We first define the lattice mismatch parameter, ε_m, for the system following Ref.[11]:

$$\varepsilon_m = \frac{a_{PbS} - a_{MAPI}}{a_{MAPI}} . \qquad (1)$$

Here, a_{PbS} and a_{MAPI} are the bulk, unstrained lattice parameters of bulk PbS and MAPI, respectively. In the case of MAPI, we use the quasi-cubic lattice parameters; our calculations are based on the tetragonal structure measured at 300K for solution-processed MAPI as reported in Ref.[12] Using the lattice parameter values given in **Table S4**, we calculate a mismatch $\varepsilon_m = -5.3\%$. The negative mismatch indicates that to achieve lattice matching at the interface, the MAPI matrix must be compressed (negative strain), since the lattice parameter of PbS is less than that of the MAPI matrix. Following Ref.,[11] the strain in the PbS QD is found to uniform and hydrostatic, with a value in the radial (ρ), and tangential (θ, ϕ) directions given by,

$$\varepsilon_{PbS} = \varepsilon_\rho = \varepsilon_\theta = \varepsilon_\phi = \varepsilon_m \left(\frac{1}{\gamma} - 1\right), \qquad (2)$$

where the mismatch parameter ε_m is given above in Eq.1, and the term $(1/\gamma - 1)$ represents the fraction of the mismatch that is accommodated by the PbS inclusion. Here, the parameter γ depends on the bulk modulus K_{PbS} and K_{MAPI} of the PbS and MAPI, respectively, and Poisson's ratio, ν_{MAPI}, for the MAPI matrix, as:[11]

$$\gamma = 1 + \frac{2K_{MAPI}(1 - 2\nu_{MAPI})}{K_{PbS}(1 + \nu_{MAPI})} . \qquad (3)$$

It is clear that as the ratio of the bulk moduli of the matrix and the inclusion (MAPI and PbS in our problem) is reduced, less of the lattice mismatch is accommodated by the inclusion as intuitively expected --the softer material deforms more. Outside the outer radius, R, of the PbS inclusion, inside the MAPI matrix, the strain field is found to be non- uniform, consisting of normal strain with no shear components, whose normal components are given as follows: The normal strain in the radial direction $\varepsilon_{MAPI,\rho}$, is given as a function of radial coordinate, r, by,

$$\varepsilon_{MAPI,\rho} = -2\frac{\varepsilon_m}{\gamma}\left(\frac{R}{r}\right)^3, \qquad (4)$$

while in the two tangential directions, (θ, ϕ), the normal strains $\varepsilon_{MAPI,\theta}$, $\varepsilon_{MAPI,\phi}$ have the opposite sign:

$$\varepsilon_{MAPI,\theta} = \varepsilon_{MAPI,\phi} = +\frac{\varepsilon_m}{\gamma}\left(\frac{R}{r}\right)^3. \qquad (5)$$

The strain components inside the PbS QD and in the MAPI matrix were calculated using the parameters in Table 1, resulting in the strain profile shown in **Figure S8**. We also shown in **Figure S8** the corresponding volume dilatation $\Delta V/V$

$$\frac{\Delta V}{V} = \varepsilon_\rho + \varepsilon_\theta + \varepsilon_\phi . \qquad (6)$$
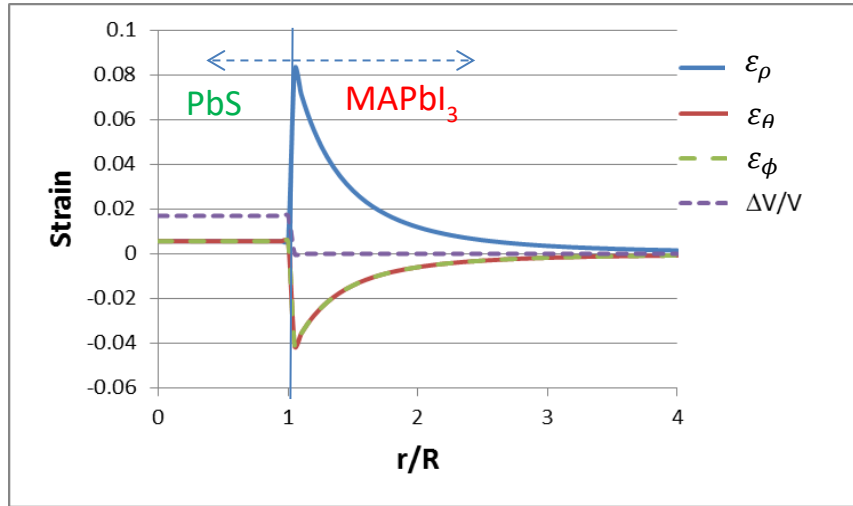
Inside the spherical PbS inclusion the three components of strain along the radial and the two tangential directions are equal in magnitude and spatially homogeneous, according to Eq. 2. The strain components are all positive, indicating tensile strain as expected since the MAPI bulk lattice constant is larger than that of PbS. As a result, the PbS inclusion is in a state of a uniform hydrostatic tension with a volume dilatation, $\Delta V/V$ of +1.7%. Outside the PbS inclusion, the two tangential components of strain are equal in magnitude, and negative, corresponding to biaxial compression of the MAPI relative to the unstrained condition. The radial component of strain in the MAPI matrix is everywhere positive, with twice the magnitude of the tangential strain, so that the volume dilatation $\Delta V/V$ in the MAPI is everywhere zero.

To determine the impact of the strain on the electronic properties of the PbS QD and the surrounding MAPI matrix, we calculated the bandgap shifts ΔE_g in both the PbS and the MAPI using the volume bandgap deformation potential for each material using the expression,

$$\Delta E_g = \alpha_V \frac{\Delta V}{V} \qquad (7)$$

Using the calculated strain shown in **Figure S9** it is clear that the bandgap of the MAPI matrix does not shift due to the strain because there is no volume dilatation in the matrix. Using the volume deformation potential for PbS given in **Table S5**, the calculated results indicate that the PbS bandgap will increase by +70 meV relative to that of unstrained bulk PbS. Unlike semiconductors such as CdSe where there band degeneracy beyond the Kramer's degeneracy, there is no conductor or valence band splitting in the MAPI due to the biaxial strain.[13]

Figure S9. Strain profile for a spherical PbS inclusion lattice matched to a surrounding MAPI matrix. The strain profiles shown are calculated using Eshelby inclusion theory following Ref.[11] using Eqs 2, 4, 5. The radial strain (ε_ρ) and two tangential components of strain (ε_θ and ε_ϕ) as well as the volume dilatation ($\Delta V/V$), Eq. 6, are plotted versus radius normalized to R, the outer radius of the PbS inclusion. Inside the spherical PbS inclusion, the three components of strain are

equal in magnitude, spatially homogeneous, and positive, indicating that the PbS inclusion is in a state of a uniform hydrostatic tensile strain with a volume dilatation of +1.7%. Outside the PbS inclusion, the two tangential components of strain are equal in magnitude, and negative, corresponding to biaxial compression. The radial component of strain is positive and equal to twice the magnitude of the tangential strain, so that the volume dilatation in the MAPI is zero. Lattice parameters and elastic constants used in this calculation are given in **Table S4.**

Table S4. Parameters used in calculating strain and bandgap shift of PbS QD in MAPI Matrix

Parameter	PbS	Ref	MAPI	Notes
Lattice constant (nm)	0.5936	T=300K, Ref.[14]	0.629	Quasi-cubic value, T=300K, Ref.[12]
Bulk modulus K (GPa)	60	Ref.[15]	13.9	Ref.[16]
Poisson's ratio ν	n/a	n/a	0.33	Ref.[16]
Bandgap volume deformation potential α_V (eV)	4.1	Ref.[15]	n/a	n/a

Quantum size level model for PbS QDs.

One-band effective mass model with infinite barrier

The simplest model for the size dependence of the absorption energy for the lowest energy exciton in colloidal PbS can be constructed within a spherical QD/ infinite barrier approximation. In a simple one-band effective mass model, the envelope functions of the ground confined carrier S-levels are given by,

$$\psi_s = A\, j_0(k\,r) Y_0^0(\theta, \phi), \qquad (8)$$

where the pre-factor A is a normalization constant, j_0 is a spherical Bessel function j_l of order $l = 0$, and $Y_0^0(\theta, \phi)$ is the spherical harmonic corresponding to $l = 0$ as appropriate for an S-state. The corresponding energies are determined by the boundary condition that the envelope function vanish at the surface of the QD, defined as radius R. This leads to the familiar expression for the energy of the lowest conduction band S-state:

$$E_S^c(R) = E_c + \frac{\hbar^2}{2m_c}\left(\frac{\pi}{R}\right)^2, \qquad (9)$$

where E_c is the energy of the conduction band (CB) edge in the bulk material and m_c is the conduction band effective mass. The energy of the highest energy occupied confined valence band (VB) state is similarly,

$$E_S^v(R) = E_v - \frac{\hbar^2}{2m_v}\left(\frac{\pi}{R}\right)^2, \qquad (10)$$

where the bulk valence band edge is denoted E_v and m_v is the valence band effective mass. The corresponding S-exciton transition energy, which would be measured as the energy of absorption from the S-level in the valence band to the S-level in the conduction band is then given by,

$$E_{exS}(R) = E_S^c(R) - E_S^v(R) = E_g + \frac{\hbar^2}{2\mu} \left(\frac{\pi}{R}\right)^2. \quad (11)$$

In the last expression, μ is the reduced effective mass, $1/\mu = 1/m_c + 1/m_v$, and E_g is the bulk band gap.

The description above, while very simple, is known to give a very poor description of the absorption energy of the S exciton in narrow gap semiconductors like PbS due to the non-parabolic band dispersion which originates from the inter-band coupling which is not accounted for in this simple model.[17] Moreover, it does not account for wavefunction leakage into the barrier region, which must be accounted for in a model of PbS QDs embedded in a MAPI matrix. We address these issues using a coupled band model for finite barrier heterostructures in the next sections.

Two-band $K \cdot P$ $model$ for a bulk semiconductor

An accurate description of the exciton energy must take account of the effect of inter-band coupling between the conduction band and valence band states in a spherical QD which gives to a non-parabolic band dispersion. The simplest model that can describe the band coupling and resulting non parabolicity is the 2-band $K \cdot P$ model. In Refs.[18,19] it is shown that the $K \cdot P$ Hamiltonian can be written in a spherical wave basis in the form,

$$H(k) = \begin{pmatrix} E_c & -i\hbar \dfrac{k\,P}{\sqrt{3}} \\ i\hbar \dfrac{k\,P}{\sqrt{3}} & E_v \end{pmatrix}. \quad (12)$$

where k is the radial wavenumber, and P is the Kane momentum matrix element: $P = -i < S|p|Z >$.[19] The $K \cdot P$ Hamiltonian above has the same representation whether written for conduction band S-states, or valence band S-states. In the former case the basis in which this Hamiltonian is written is comprised of spherical waves angular momentum $l = 0$ in the conduction band and $l = 1$ in the valence band, and conversely, to describe the S-states in the valence band the appropriate basis consists of a spherical wave with $l = 0$ in the valence band and one with $l = 1$ in the conduction band. Inherent in the description is the fact that away from the band edges, with non-zero radial momentum k, the S and P conduction and valence band states are coupled.[17–19] It is important to note that Eq. 12 is very similar to Hamiltonian derived by Kang and Wise.[17] but has the feature that it does not contain terms on the diagonal that go as K^2 which are known to give rise to non-physical solutions with large imaginary wave vector. Diagonalization of the

Hamiltonian, Eq. 12, gives the following expression for the band dispersion in the material in the vicinity of the conduction and valence band edges, which is hyperbolic rather than parabolic:

$$(E - E_c)(E - E_v) = \frac{\hbar^2}{2m_0} \frac{E_p}{3} \quad , \qquad (13)$$

where E_p is the Kane energy, given in terms of the momentum matrix element for the material and the free electron mass m_0 by,

$$E_p = 2\,P^2/m_0 \quad , \qquad (14)$$

The band edge effective masses of the conduction and valence band, m_c and m_v, respectively, are equal: $m_c = m_v = m^*$, where m^* is given by,

$$\frac{m^*}{m_0} = \frac{3\,E_g}{E_p} \quad . \qquad (15)$$

Coupled band effective mass model for a spherical QD-in matrix: Finite barrier model

In order to model the QD- in-matrix samples investigated in this study, we applied the Kane 2-band model discussed above to the radial heterostructure formed by the PbS QD inside the MAPI matrix barrier material. As before, the PbS QDs are assumed to be spherically shaped. Our model for the heterointerface is shown in **Figure S10**. The band offsets shown there are derived from the measured bulk ionization potentials and the bandgaps of PbS and MAPI, as summarized in **Table S5,** corresponding to a Type-1 band alignment. The effect of strain as reflected in the calculation shown in **Figure S9** is included as well, using the deformation potentials in **Table S4**, and assuming that the PbS CB and VB edges shift equally under the hydrostatic strain. To model the quantum confined levels in this system we used the finite barrier model developed in Refs.[18,19] There it is shown that the S-states of the conduction band can be described by states written in a vector form, with radial functions represented inside and outside the QD by,

$$\psi^{in}(r) = A \begin{pmatrix} j_0(kr) \\ \Theta_{in} j_l(kr) \end{pmatrix} \qquad \psi^{out}(r) = B \begin{pmatrix} h_0(\lambda r) \\ \Theta_{out} h_l(\lambda r) \end{pmatrix} \quad . \qquad (16)$$

Here, subscripts in/out refer to the regions inside and outside the PbS QD respectively, j_l is a spherical Bessel function order l, while h_l is the spherical Hankel function of imaginary argument and order l that decays for large r. The radial wave numbers k and λ and given by the band dispersion relations inside and outside the QD, by

$$\left(E - E_{c,in}\right)\left(E - E_{v,in}\right) = \frac{\hbar^2}{2m_0} \frac{E_{p,in}}{3} k^2 \qquad (17)$$

$$\left(E - E_{c,out}\right)\left(E - E_{v,out}\right) = -\frac{\hbar^2}{2m_0} \frac{E_{p,out}}{3} \lambda^2 \quad . \qquad (18)$$

Note that the radial wavenumber in the outside region (the MAPI barrier) is taken to be $k_{MAPI} = i\lambda$ in anticipation of finding bound solutions whose energy lies within the MAPI bandgap. Finally, the terms $\Theta_{in/out}$ are given by,

$$\Theta_{in} = -i\,\frac{\hbar}{m_0}\frac{k\,P_{in}}{\sqrt{3}\,\left(E_v^{in} - E\right)};\qquad \Theta_{in} = -\,\frac{\hbar}{m_0}\frac{\lambda\,P_{out}}{\sqrt{3}\,\left(E_v^{out} - E\right)}\,.\qquad(19)$$

The energy of the lowest conduction band state is given by solving the system of equations formed by Eq 17 and 18 above, plus one additional equation derived from requiring continuity of the wave function at the QD/MAPI interface at radius $r = R$:

$$\frac{j_0(k\,R)h_1(i\lambda R)}{j_1(k\,R)h_0(i\lambda R)} = \frac{-i\,k}{\lambda}\frac{\left(E - E_v^{out}\right)}{\left(E - E_v^{in}\right)}\,.\qquad(20)$$

For the valence band state the corresponding analysis leads to the equation,

$$\frac{j_0(k\,R)h_1(i\lambda R)}{j_1(k\,R)h_0(i\lambda R)} = \frac{-i\,k}{\lambda}\frac{\left(E_c^{out} - E\right)}{\left(E_c^{in} - E\right)}\,.\qquad(21)$$

The energies of the exciton absorption versus QD radius in **Fig. 6** of the main text are calculated by solving these expressions for a given QD radius R using the material parameters summarized
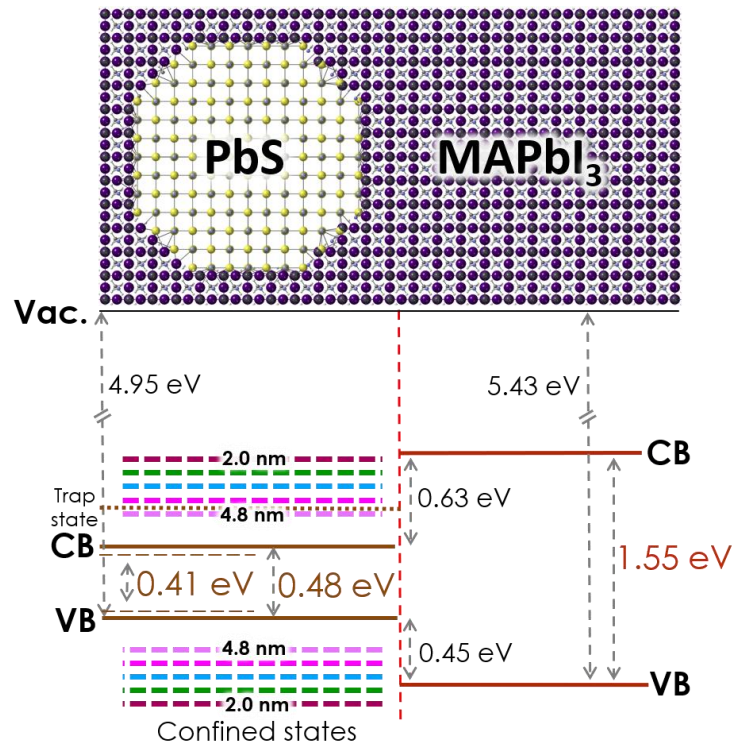
Figure S10. Model for the PbS/MAPI interface. The band CB and VB band alignments are drawn based on the measured bulk ionization potentials for PbS and MAPI taken from Refs McDonald[20]

and Kim,[21] respectively, and the bulk band gaps as listed in **Table S5**, corresponding to type-1 band alignment. The strain associated with the lattice mismatch is accounted for in this model using the lattice constants, elastic parameters, and the deformation potential listed in **Table S5** along with the strain calculation shown in **Figure S9**. The PbS quantum dot experiences hydrostatic strain causing a band gap increase of 70 meV; the bandgap increase is assumed to be equally distributed in the conduction and valence band edges. The resulting CB and VB offsets are ΔE_c= 0.625 eV; and ΔE_v= 0.445 eV, respectively. The colored dashed lines in the PbS band diagram represent the confined band edge states as the QD size changes.

in **Table S5**. The exciton energy for a given radius is then simply the difference in energy between the lowest energy CB and VB quantum size levels found in this manner.

Table S5: Model parameters for PbS colloidal QDs and PbS QDs in MAPI matrix.

Parameter	PbS	Notes/Ref	MAPI	Notes/Ref
E_g (300K) (eV)	0.41	Ref.[17]	1.55	Measured (this work)
E_p (eV)	13.7	This work, from fit to absorption data in Fig. 6	17.2	Calculated using Eq.15 from m* in Ref.[22]
m* band edge	0.09	Calculated using Eq 15 with E_g, E_p above	0.27	Ref.[22]
Ionization potential (eV)	4.95	Ref.[23]	5.43	Ref.[21]
Deformation potential (eV)	4.1	Ref.[15]	n/a	

Coupled band effective mass model for a colloidal QD- infinite barrier model

To model the absorption of colloidal PbS QDs, we applied the 2-band $K \cdot P$ model developed above, but in contrast to the case of the QD-in-matrix analysis, we do so in the limit of an infinite potential barrier at the QD surface. This limit is realized if, in Eqs. 19-21, we take the band gap in the outside region to be infinite. We follow the analysis developed in the Supplementary Material of Ref.[19]. There, it is shown that in this limit, the surface boundary condition for the conduction band S-state, Eq. 21, takes the form,[19]

$$\frac{j_0(k\,R)}{j_1(k\,R)} = \sqrt{\frac{\hbar^2}{2m_0}\frac{E_p}{3}\frac{k}{(E - E_v)}} \quad . \qquad (22)$$

For the valence band state, the surface boundary condition, Eq. 21 goes to,

$$\frac{j_0(k\,R)}{j_1(k\,R)} = \sqrt{\frac{\hbar^2}{2m_0}\frac{E_p}{3}\frac{k}{(E_c - E)}} \quad . \qquad (23)$$

To find the energy of the lowest S-state in the CB or the VB, these equations are solved along with Eq. 17 for the band dispersion inside the QD. We note that if we reference the conduction band S-state energy to the conduction band edge $E_S(R) = E - E_c$ then Eq. 22 can be written,

$$\frac{j_0(k\,R)}{j_1(k\,R)} = \sqrt{\frac{\hbar^2}{2m_0}\frac{E_p}{3}}\frac{k}{\left(E_S(R) + E_g\right)} \quad . \qquad (24)$$

Similarly, Eq. 17 transforms to,

$$E_S(R)\{E_S(R) + E_g\} = \frac{\hbar^2}{2m_0}\frac{E_p}{3} \quad . \qquad (25)$$

If we similarly reference the valence band S-state energy to the bulk valence band edge, $E_S = E_v - E$ we obtain the identical equations. This shows that the energy of the confined electron and the confined hole relative to their respective band edges are equal, as expected in a 2-band Kane model where the conduction and valence band effective masses are equal. Thus, the exciton energy in this model relative to the band gap is simply,

$$E_{exS}(R) = E_g + 2\,E_S(R), \qquad (26)$$

where the carrier confinement energy $E_S(R)$ is found by simultaneously solving Eqs. 24 and 25. To determine the model parameters, the measured absorption energy of the colloidal PbS versus size was fitted with this model using the bulk room temperature band gap of PbS $E_g^{PbS} = $ 410meV[17] and optimizing the parameter E_p in order to match the measured absorption energy versus size. The fitted value is given in **Table S5.** The resulting fit to the measured exciton absorption energy, shown in **Figure 6** of the main text, is excellent. The fit in **Figure 6** was performed for the PbS QDs samples grown with PbO precursor, but as shown in **Figure 6** the model works equally well for the colloidal samples grown with Cl precursor.

Model for photoluminescence emission Stokes shift

As shown in the main text, the PL emission energy shows a significant size-dependent Stokes shift relative to the absorption energy for a given size PbS QD both in the measurements performed on colloidal PbS QDs as well as in PbS/MAPI QD-in-matrix samples measured during the course of this study. For the colloidal PbS QDs, we attribute the Stokes shift to emission occurring on a transition from an electron defect or interface state at energy E_t ~250 meV above the bulk conduction band edge to the confined hole state in the valence band (VB), following models previously proposed for the PL emission in colloidal PbS QDs.[24,25] Therefore, the emitting state in the CB becomes pinned for small sized NCs while only the movement of the VB confined level as the QD size changes influences the shift in PL emission energy with the QD size, as depicted schematically in **Figure S11**. This model accounts quantitatively for the observed size-dependent

PL Stokes shift as shown in **Figure 6** of the main text, with only a single fit parameter, the energy of the trap level above the bulk PbS conduction band edge.

In the PbS QDs grown in MAPI, the confined electron and hole states are also described within a coupled band Kane model as are the colloidal PbS QDs, but in contrast to the colloidal PbS QDs, the QD surface is described within a finite barrier model for the PbS/MAPI interface as detailed above. Nevertheless, using the same energy for the electron trap depicted schematically in **Figure S11**, namely, 250 meV above the bulk unstrained conduction band (CB) edge, this model again accounts quantitatively for the PL emission energy from the smaller sized PbS QDs in MAPI measured in this study. For the larger sized PbS QDs in MAPI, there is variation from sample to sample in the PL Stokes shift, which as described in the main text, may be consistent with formation of interface dislocations in the larger QDs samples. This would cause shifts in the absorption and PL energy due to variation in the strain due to relaxation via dislocation formation and would potentially affect PL as well by introduction of new interface states.
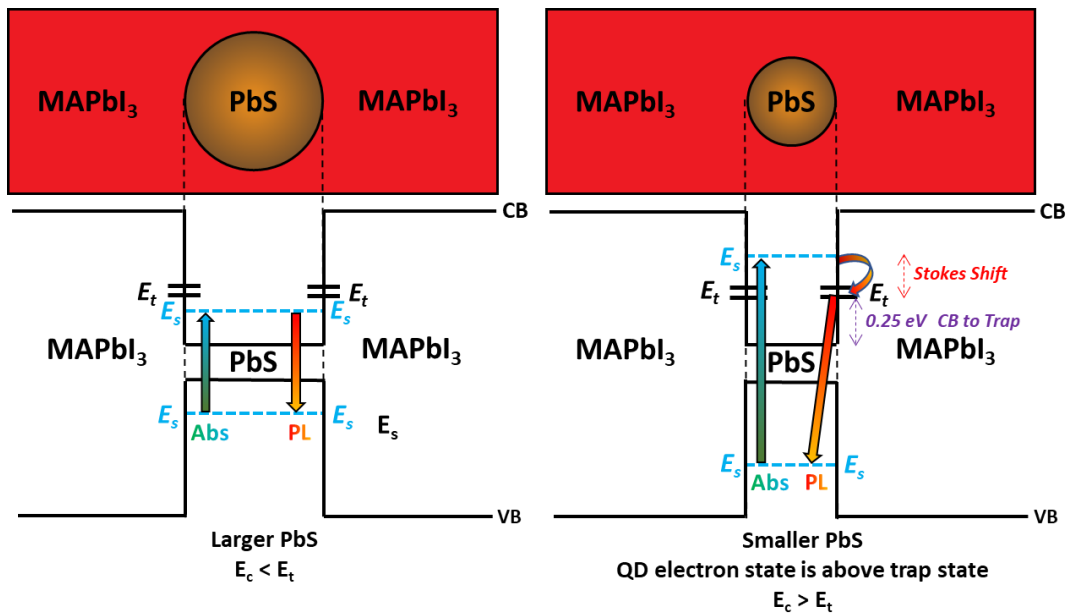
Figure S11. Schematic depicting the origin of the PL Stokes shift in PbS QDs. For large sized QDs, left, the confined electron state at energy E_S is at an energy lower than the electron trap, at energy E_t, and there is minimal Stokes shift. For small QDs, the electron confined state is at a higher energy than the trap state, so that following absorption, non-radiative relaxation of the electron to the trap occurs. Subsequently, PL emission from the trap state to the confined valence band state occurs, resulting in a size-dependent Stokes shift. The model explains the PL in both colloidal PbS QDs as well as in the small-sized PbS/MAPI QD-in-matrix samples, using the same energy position for the posited electron trap level, 250 meV above the conduction band edge of bulk PbS.

References

(1)   Hines, M. A.; Scholes, G. D. Colloidal PbS Nanocrystals with Size-Tunable Near-Infrared Emission: Observation of Post-Synthesis Self-Narrowing of the Particle Size Distribution. *Adv. Mater.* **2003**, *15*, 1844–1849. https://doi.org/10.1002/adma.200305395.

(2)   Moreels, I.; Lambert, K.; Smeets, D.; De Muynck, D.; Nollet, T.; Martins, J. C.; Vanhaecke, F.; Vantomme, A.; Delerue, C.; Allan, G.; et al. Size-Dependent Optical Properties of Colloidal PbS Quantum Dots. *ACS Nano* **2009**, *3*, 3023–3030. https://doi.org/10.1021/nn900863a.

(3)   Zhang, J.; Gao, J.; Miller, E. M.; Luther, J. M.; Beard, M. C. Diffusion-Controlled Synthesis of PbS and PbSe Quantum Dots with in Situ Halide Passivation for Quantum Dot Solar Cells. *ACS Nano* **2014**, *8*, 614–622. https://doi.org/10.1021/nn405236k.

(4)   Dirin, D. N.; Dreyfuss, S.; Bodnarchuk, M. I.; Nedelcu, G.; Papagiorgis, P.; Itskos, G.; Kovalenko, M. V. Lead Halide Perovskites and Other Metal Halide Complexes As Inorganic Capping Ligands for Colloidal Nanocrystals. *J. Am. Chem. Soc.* **2014**, *136*, 6550–6553. https://doi.org/10.1021/ja5006288.

(5)   Sytnyk, M.; Yakunin, S.; Schöfberger, W.; Lechner, R. T.; Burian, M.; Ludescher, L.; Killilea, N. A.; YousefiAmin, A.; Kriegner, D.; Stangl, J.; et al. Quasi-Epitaxial Metal-Halide Perovskite Ligand Shells on PbS Nanocrystals. *ACS Nano* **2017**, *11*, 1246–1256. https://doi.org/10.1021/acsnano.6b04721.

(6)   Harvey, S. P.; Messinger, J.; Zhu, K.; Luther, J. M.; Berry, J. J. Investigating the Effects of Chemical Gradients on Performance and Reliability within Perovskite Solar Cells with TOF-SIMS. *Adv. Energy Mater.* **2020**, *1903674*, 1903674. https://doi.org/10.1002/aenm.201903674.

(7)   Harvey, S. P.; Zhang, F.; Palmstrom, A.; Luther, J. M.; Zhu, K.; Berry, J. J. Mitigating Measurement Artifacts in TOF-SIMS Analysis of Perovskite Solar Cells. **2019**. https://doi.org/10.1021/acsami.9b09445.

(8)   Harvey, S. P.; Li, Z.; Christians, J. A.; Zhu, K.; Luther, J. M.; Berry, J. J. Probing Perovskite Inhomogeneity beyond the Surface: TOF-SIMS Analysis of Halide Perovskite Photovoltaic Devices. *ACS Appl. Mater. Interfaces* **2018**, *10*, 28541–28552. https://doi.org/10.1021/acsami.8b07937.

(9)   Ning, Z.; Gong, X.; Comin, R.; Walters, G.; Fan, F.; Voznyy, O.; Yassitepe, E.; Buin, A.; Hoogland, S.; Sargent, E. H. Quantum-Dot-in-Perovskite Solids. *Nature* **2015**, *523*, 324–328. https://doi.org/10.1038/nature14563.

(10)   Eshelby, J. D. The Determination of the Elastic Field of an Ellipsoidal Inclusion, and Related Problems. *Proc. R. Soc. London. Ser. A. Math. Phys. Sci.* **1957**, *241*, 376–396. https://doi.org/10.1098/rspa.1957.0133.

(11)   Yang, M.; Sturm, J. C.; Prevost, J. Calculation of Band Alignments and Quantum Confinement Effects in Zero- and One-Dimensional Pseudomorphic Structures. *Phys. Rev. B* **1997**, *56*, 1973–1980. https://doi.org/10.1103/PhysRevB.56.1973.

(12)   Kong, W.; Ye, Z.; Qi, Z.; Zhang, B.; Wang, M.; Rahimi-Iman, A.; Wu, H. Characterization of an Abnormal Photoluminescence Behavior upon Crystal-Phase Transition of Perovskite

CH3NH3PbI3. *Phys. Chem. Chem. Phys.* **2015**, *17*, 16405–16411. https://doi.org/10.1039/c5cp02605a.

(13)   Bir, G. L.; Pikus, G. E. *Symmetry and Strain-Induced Effects in Semiconductors*; Wiley, 1974.

(14)   Madelung, O.; Rössler, U.; Schulz, M. *Lead Sulfide (PbS) Crystal Structure, Lattice Parameters, Thermal Expansion*; Springer-Verlag: Berlin/Heidelberg, 1998. https://doi.org/10.1007/10681727_889.

(15)   Rabii, S. Investigation of Energy-Band Structures and Electronic Properties of PbS and PbSe. *Phys. Rev.* **1968**, *167*, 801–808. https://doi.org/10.1103/PhysRev.167.801.

(16)   Rakita, Y.; Cohen, S. R.; Kedem, N. K.; Hodes, G.; Cahen, D. Mechanical Properties of APbX3 (A = Cs or CH 3 NH 3 ; X = I or Br) Perovskite Single Crystals. *MRS Commun.* **2015**, *5*, 623–629. https://doi.org/10.1557/mrc.2015.69.

(17)   Kang, I.; Wise, F. W. Electronic Structure and Optical Properties of PbS and PbSe Quantum Dots. *J. Opt. Soc. Am. B* **1997**, *14*, 1632. https://doi.org/10.1364/JOSAB.14.001632.

(18)   Sercel, P. C.; Vahala, K. J. Analytical Formalism for Determining Quantum-Wire and Quantum-Dot Band Structure in the Multiband Envelope-Function Approximation. *Phys. Rev. B* **1990**, *42*, 3690–3710. https://doi.org/10.1103/PhysRevB.42.3690.

(19)   Sercel, P. C.; Lyons, J. L.; Bernstein, N.; Efros, A. L. Quasicubic Model for Metal Halide Perovskite Nanocrystals. *J. Chem. Phys.* **2019**, *151*, 234106. https://doi.org/10.1063/1.5127528.

(20)   McDonald, S. A.; Konstantatos, G.; Zhang, S.; Cyr, P. W.; Klem, E. J. D.; Levina, L.; Sargent, E. H. Solution-Processed PbS Quantum Dot Infrared Photodetectors and Photovoltaics. *Nat. Mater.* **2005**, *4*, 138–142. https://doi.org/10.1038/nmat1299.

(21)   Kim, H.-S.; Lee, C.-R.; Im, J.-H.; Lee, K.-B.; Moehl, T.; Marchioro, A.; Moon, S.-J.; Humphry-Baker, R.; Yum, J.-H.; Moser, J. E.; et al. Lead Iodide Perovskite Sensitized All-Solid-State Submicron Thin Film Mesoscopic Solar Cell with Efficiency Exceeding 9%. *Sci. Rep.* **2012**, *2*, 591. https://doi.org/10.1038/srep00591.

(22)   Mosconi, E.; Umari, P.; De Angelis, F. Electronic and Optical Properties of MAPbX 3 Perovskites (X = I, Br, Cl): A Unified DFT and GW Theoretical Analysis. *Phys. Chem. Chem. Phys.* **2016**, *18*, 27158–27164. https://doi.org/10.1039/C6CP03969C.

(23)   McDonald, S. A.; Konstantatos, G.; Zhang, S.; Cyr, P. W.; Klem, E. J. D.; Levina, L.; Sargent, E. H. Solution-Processed PbS Quantum Dot Infrared Photodetectors and Photovoltaics. *Nat. Mater.* **2005**, *4*, 138–142. https://doi.org/10.1038/nmat1299.

(24)   Fernée, M. J.; Thomsen, E.; Jensen, P.; Rubinsztein-Dunlop, H. Highly Efficient Luminescence from a Hybrid State Found in Strongly Quantum Confined PbS Nanocrystals. *Nanotechnology* **2006**, *17*, 956–962. https://doi.org/10.1088/0957-4484/17/4/020.

(25)   Ushakova, E. V.; Litvin, A. P.; Parfenov, P. S.; Fedorov, A. V.; Artemyev, M.; Prudnikau, A. V.; Rukhlenko, I. D.; Baranov, A. V. Anomalous Size-Dependent Decay of Low-Energy Luminescence from PbS Quantum Dots in Colloidal Solution. *ACS Nano* **2012**, *6*, 8913–8921. https://doi.org/10.1021/nn3029106.